Swarm and ESR observations of the ionospheric response to a field-aligned current system in the high-latitude midnight sector

F. Pitout[1,2], A. Marchaudon[1,2], P.-L. Blelly[1,2], X. Bai[1,2], F. Forme[1,2], S. C. Buchert[3], and D. A. Lorentzen[4,5]

[1]UPS-OMP, IRAP, Université de Toulouse, Toulouse, France, [2]CNRS, IRAP, Toulouse, France, [3]Swedish Institute for Space Physics, Uppsala, Sweden, [4]University Centre in Svalbard, Longyearbyen, Norway, [5]Birkeland Centre for Space Science, University Centre in Svalbard, Longyearbyen, Norway

Abstract We present a conjunction between the Swarm fleet and the European Incoherent Scatter Svalbard Radar (ESR) on 9 January 2014. The Swarm orbit in the early phase of the mission gives us the unique opportunity of sequencing the temporal evolution of the observed field-aligned current system in the nightside, near magnetic local midnight. These field-aligned currents are seen to move poleward through the radar field of view and to affect the observed ionosphere. The upward field-aligned current (FAC) is responsible, at least in part, for the heating of the ionospheric electrons. It is less clear whether the downward FAC cools the ionosphere. We use the TRANSCAR model of the ionosphere to quantify the thermoelectric effect that comes into play. Finally, we compare the plasma parameters measured by the Langmuir probe on board Swarm and the ESR and conclude on an agreement within the errors.

1. Introduction

1.1. Large- and Small-Scale Field-Aligned Currents

Field-aligned currents (hereinafter referred to as FAC) are an effective way to couple the magnetosphere to the ionosphere; indeed, they contribute to the transfer of energy and momentum between the two media. There exists a large-scale FAC system (also known as Birkeland currents), which includes the Region 1 FAC that couple the external magnetosphere current to the high-latitude ionosphere and the Region 2 FAC that couple the inner magnetosphere to the auroral ionosphere. These large-scale current systems have been widely reported and documented in statistical work using single spacecraft [e.g., *Iijima and Potemra*, 1976] and satellite constellations [*Anderson et al.*, 2008]. More recently, near-instantaneous global distributions of the FACs have been inferred by the Active Magnetosphere and Planetary Electrodynamics Response Experiment (AMPERE) [*Anderson et al.*, 2014].

In addition to the large-scale currents systems, FACs with smaller spatial scales are also observed. They may be associated, for instance, with dayside phenomena such as the injection of solar wind plasma in the dayside magnetosphere and ionosphere [*Marchaudon et al.*, 2006, 2009] or field line resonance [*Pitout et al.*, 2003]. They also occur, as discussed in this paper, in the nightside when a substorm develops [*Iijima and Potemra*, 1978] or associated with a solar wind pressure pulse [*Winglee and Menietti*, 1998].

1.2. Ionospheric Effects of Field-Aligned Currents

More than their cause, it is the effects of FAC in the ionosphere we are interested in. It is well known that FAC close in the ionosphere mainly through Pedersen currents. Being parallel to the electric field, Perdersen currents are dissipative and contribute to the transfer of energy from the magnetosphere to the ionosphere. However, this is not the only way for transferring energy. As they flow through the ionosphere, FACs also deposit energy in or absorb energy from the ionosphere, depending on their direction, via the thermoelectric effect: upward FACs correspond to a downward electron heat flux and warm up the ionospheric electrons, whereas downward FAC are accompanied by an upward electron heat flux and thus cool down the ionospheric electrons [*Banks et al.*, 1976; *Blelly and Alcaydé*, 1994; *Blelly et al.*, 1996]. FACs are therefore expected to play a crucial role in the thermodynamics of the high-latitude ionosphere.

2. Observations and Interpretation

2.1. Instrumentation

We take advantage in this study of a fortunate conjunction between the Swarm satellites and the European Incoherent Scatter (EISCAT) Svalbard Radar (ESR).

Swarm [*Friis-Christensen et al.*, 2008] is a European Space Agency mission designed to study the Earth's magnetic field. It consists of three identical satellites, which accommodate a comprehensive payload designed to measure the magnetic field of course, but also all the features that can locally modify the magnetic field. That is the reason why there are on board accelerometers, Langmuir probes, and ion sensors. In its early phase, i.e., before the spacecraft reached their nominal orbits, the Swarm mission was in a string-of-pearl configuration: the three satellites were flying in the same circular near-polar orbit (inclination 87.55°), one after the other. Swarm B, the leading spacecraft, and Swarm A are separated by about 530 km along their track, and Swarm A and Swarm C, the trailing satellite, by about 960 km, which correspond to 1 min 17 s and 2 min 21 s flight time, respectively. The other difference with their final orbits is their common altitude: approximately 500 km for all three satellites.

The EISCAT Svalbard Radar (ESR) is the northernmost radar system of the European Incoherent SCATter (EISCAT) scientific association [*Röttger et al.*, 1995]. It is located on the Spitzbergen Island at 78.15° geographic latitude and 16.02° geographic longitude. It transmits a radio signal in the UHF band at 500 MHz, and from the backscattered signal, one can infer physical ionospheric parameters such as the electron number density, the electron and ion temperatures, and the line of sight ion velocity. The system consists of two antennas: one fixed and pointing along the local magnetic field line, the second is fully steerable.

Swarm B, A, and C satellites, coming from the high-latitude polar cap, flew southward in this order in the close vicinity of the ESR beam. The closest point to the center of the radar beam at 500 km altitude was reached at 20:25:25 UT by Swarm B (19 km off), at 20:26:42 UT by Swarm A (12 km), and at 20:29:03 UT by Swarm C (3 km). Considering the width of the beam (0.6° at −3 dB, equivalent to 10 km at 500 km), Swarm C flew right through the beam while Swarms A and B passed on the east side.

We also use the International Monitor for Auroral Geomagnetic Effects (IMAGE) magnetometer network in Scandinavia [*Lühr*, 1994], the Meridian Scanning Photometer (MSP) installed near the ESR site at the Kjell Henriksson Observatory to monitor the auroral activity, and the Super Dual Auroral Radar Network (SuperDARN) network [*Greenwald et al.*, 1995] of coherent scatter radars to monitor the ionospheric convection.

2.2. Context and Timing of the Event

We focus in this paper on 9 January 2014 between 20:00 and 21:00 UT. During this time interval, the prevailing solar wind and interplanetary magnetic field (IMF) conditions are given by the Artemis spacecraft [*Angelopoulos*, 2008, 2011]. Artemis P1 located at $(X, Y, Z)_{GSE} \sim (-21, 59, 0) R_E$ observes (Figures 1a and 1b) the arrival of a solar wind discontinuity at 20:12 UT: the solar wind dynamic pressure increased from 1 to 4 nPa. The Z_{GSM} component of the interplanetary magnetic field (IMF), which plays a crucial role in the solar wind-magnetosphere coupling, remains slightly positive during the whole time. It has to be noted, however, that the Y_{GSM} component measured around −5 nT but decreased to −15 nT after the arrival of the discontinuity and may thus act as a reconnecting component and actually couple effectively the IMF and the Earth's magnetic field [e.g., *Trattner et al.*, 2012]. The X component remains between −5 nT and 0 nT throughout the event.

The exact impact time of the discontinuity on the magnetosphere is given by the Time History of Events and Macroscale Interactions during Substorms (THEMIS-E) satellite which was close to the dayside magnetopause at $(X, Y, Z)_{GSE} \sim (8, 7, 1) R_E$, inside the magnetosphere, just before the pressure pulse arrived. Following the compression of the magnetosphere, THEMIS-E found itself in the magnetosheath at 20:11:30 UT where it recorded the shocked IMF (not shown).

The overall high-latitude geomagnetic activity can be monitored by the *AE* index whose provisional value is shown in Figure 1c. *AE* index starts to increase at 20:12 UT and reaches a maximum of 551 nT ($AU = 47$ nT; $AL = -504$ nT) at 20:16 UT. It appears that the *AE* values come mainly from the European sector. Indeed, the whole IMAGE network records as soon as 20:12 UT a slight decrease in the northward component of
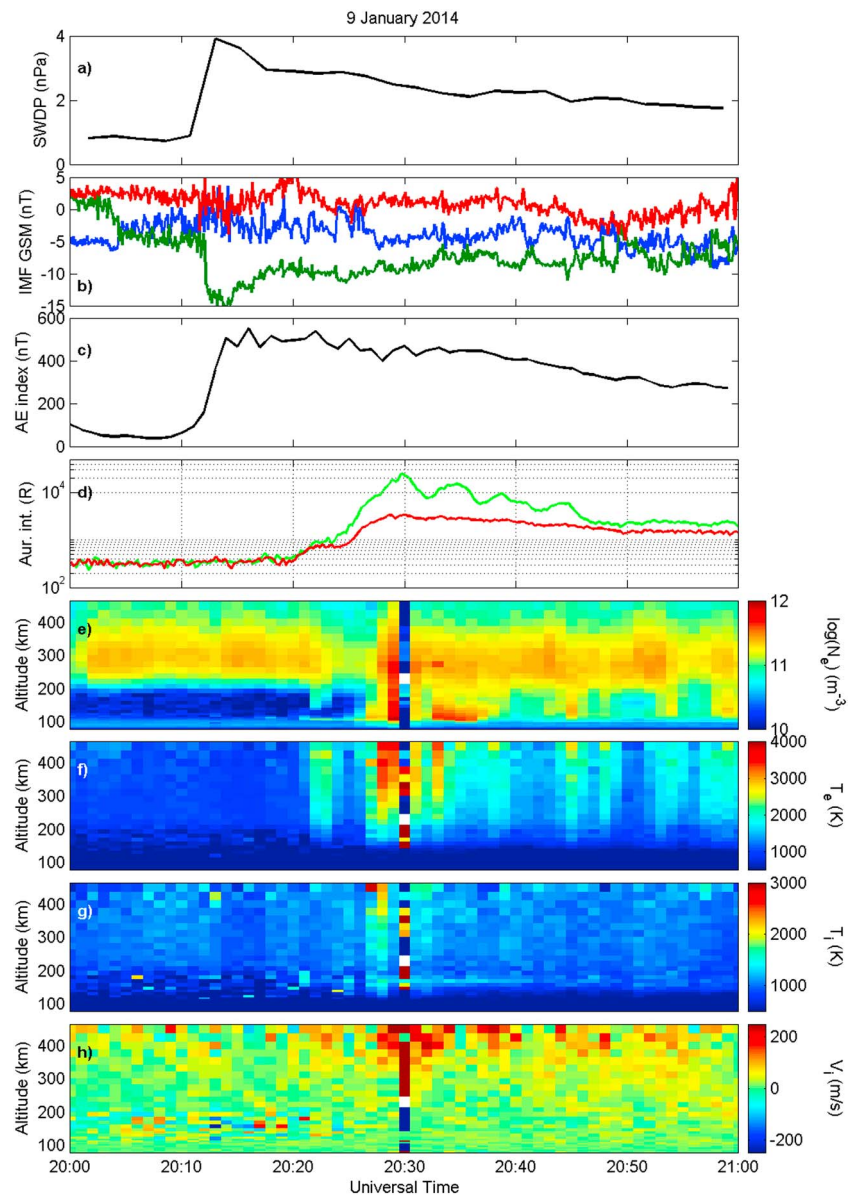
Figure 1. The external conditions and geophysical context with (a) the solar wind dynamic pressure measured by the electrostatic analyzer instrument on board Artemis P1, (b) the three GSM components of interplanetary magnetic field recorded by the FluxGate Magnetometer instrument on board Artemis P1 (Bx, By, and Bz are blue, green, and red, respectively), (c) the AE index, and (d) the field-aligned integrated intensity of the atomic oxygen red and green lines measured by the MSP. The ESR data with (e) the electron number density, (f) the electron temperature, (g) the ion temperature, and (h) the ion field-aligned velocity, as functions of altitude and universal time.

the ground magnetic field. The most visible signature is at high latitudes where the Svalbard stations measure stronger variations from 20:20 UT as a negative deviation of the northward component, equivalent to a westward Hall current and a subsequent poleward motion of this current.

Although the sky was cloudy, the MSP records (Figure 1d) in both the atomic oxygen green and red lines a faint auroral activity starting at 20:20 UT followed by a sudden and strong auroral intensification at 20:25 UT, with maxima around 20:29 UT.

2.3. Swarm Data Analysis

The string-of-pearl configuration does not allow us to determine the FAC density by the curlometer technique [*Dunlop and Balogh*, 1993; *Robert and Roux*, 1993; *Ritter et al.*, 2013]. Yet it is worth

considering this configuration for the study of the temporal evolution of dynamical features, such as FAC precisely. Consequently, the FAC densities shown in the present work are computed with a single-spacecraft technique. This technique essentially consists of calculating a single component of curl **B** and invoking Ampere's law to infer the current density parallel to the magnetic field direction. The assumption of an infinite current sheet lying perpendicular to the satellite track has to be made, which is usually fine for large-scale current systems that have a large longitudinal extent. However, in the case of currents with smaller spatial scale, this hypothesis may lead to an incorrect estimate of the current density. In this paper, we use an improved single-spacecraft technique in the sense that we do not assume that the infinite vertical current sheet is perpendicular to the satellite track. We first search for the orientation of the current sheet with respect to the satellite track by performing an minimum variance analysis (MVA) on the 1 Hz resolution magnetic field measured by the Vector Field Magnetometer (VFM) on board the three Swarm spacecraft (Figures 2a and 2b). (For more information about Swarm data products, the reader may refer to *Olsen et al.* [2013]). Then, once the relative orientation is known, we are able to take into account the correct horizontal magnetic field to estimate the curl of **B** and thus the FAC density [*Marchaudon et al.*, 2006].

The angle Φ between the magnetic east direction and the direction along which lies the current sheet is displayed in Figure 2c. Let us emphasize that the advantages for retrieving this angle are numerous. First, it allows the overall current structure crossed by the satellite to be identified as a current sheet or not (e.g., filamentary current): if, within a structure, the angle does not vary too much, then it means that globally the crossed structure can be identified as a current sheet. Second, having the direction of the current sheet is important to find out whether the identified current structure is aligned at constant latitude or along another direction, potentially revealing complex electrodynamic structures in the ionosphere. It is often the case for structures smaller than the large-scale Region 1/Region 2 currents. Third, it is useful in our case when the three Swarm spacecraft are aligned in a string-of-pearl configuration: it allows the temporal dynamics of these structures to be followed in terms of motion and orientation.

Figure 2d shows the FAC density (counted positive upward) as a function of magnetic latitude, determined for each spacecraft. At each point (each second), the current is determined on a 7 s time interval, which is a good compromise between a smoothing effect which removes spikes and an acceptable spatial resolution to observe mesoscale structures. The errors on the FAC density take into account the systematic error on the magnetic field measurement but may come from the determination of the orientation of the current sheet (the error calculation is adapted from *Ritter et al.* [2013]). Indeed, when the angle Φ is too large (close to $\pm 90°$), then the error becomes very large (Figures 2c and 2d).

At Swarm B, a downward current is first observed south of the ESR beam, peaking at $-14 \mu A/m^2$ at 73.9° magnetic latitude and then an upward FAC of $10 \mu A/m^2$ at 73.5° magnetic latitude. About 1 min later, Swarm A starts to fly through a downward FAC at higher magnetic latitude (75.5°), reaches an extremum of $-9 \mu A/m^2$ at 75.1°, changes direction at 74.4°, and reaches a maximum of $+5 \mu A/m^2$ at 73.5°. It has to be noted that within the region of globally downward FAC, a region with no current or weakly upward is crossed near the ESR beam. As for Swarm C, it enters a region of downward FAC even at higher magnetic latitude (75.8°) with an extremum of $-7 \mu A/m^2$ at 75.2° magnetic latitude. The FAC appears to change sign at least twice between 75° and 74.6°. Then Swarm C enters in an upward FAC region south of 74.6° with an extremum of $+11 \mu A/m^2$ at 74.5° magnetic latitude. Obviously, given all the caveats discussed above and the errors made (Figure 2d), current densities obtained for an angle Φ close to $\pm 90°$ cannot be trusted; this is especially true for the higher current densities.

We can draw three conclusions out of these observations. First, all Swarm spacecraft fly through a ~ 3° wide downward/upward FAC system between 73° and 76° magnetic latitude with, globally, a downward FAC being poleward of the upward FAC. In addition to this tendency, some smaller substructures may be seen in data from Swarms A and C, substructures that do correspond to very local and abrupt variations of the magnetic field. Second, the FAC structure appears to move poleward between the crossings of Swarms B, A, and C. Third, the ESR should be sounding a region with no FAC when SWARM B passes by around 20:25 UT, a region of downward FAC (~ $-5 \mu A/m^2$ on average) when Swarm A passes around 20:26 UT, and a region of upward FAC (~ $+5 \mu A/m^2$ on average) when Swarm C flies by around 20:29 UT.
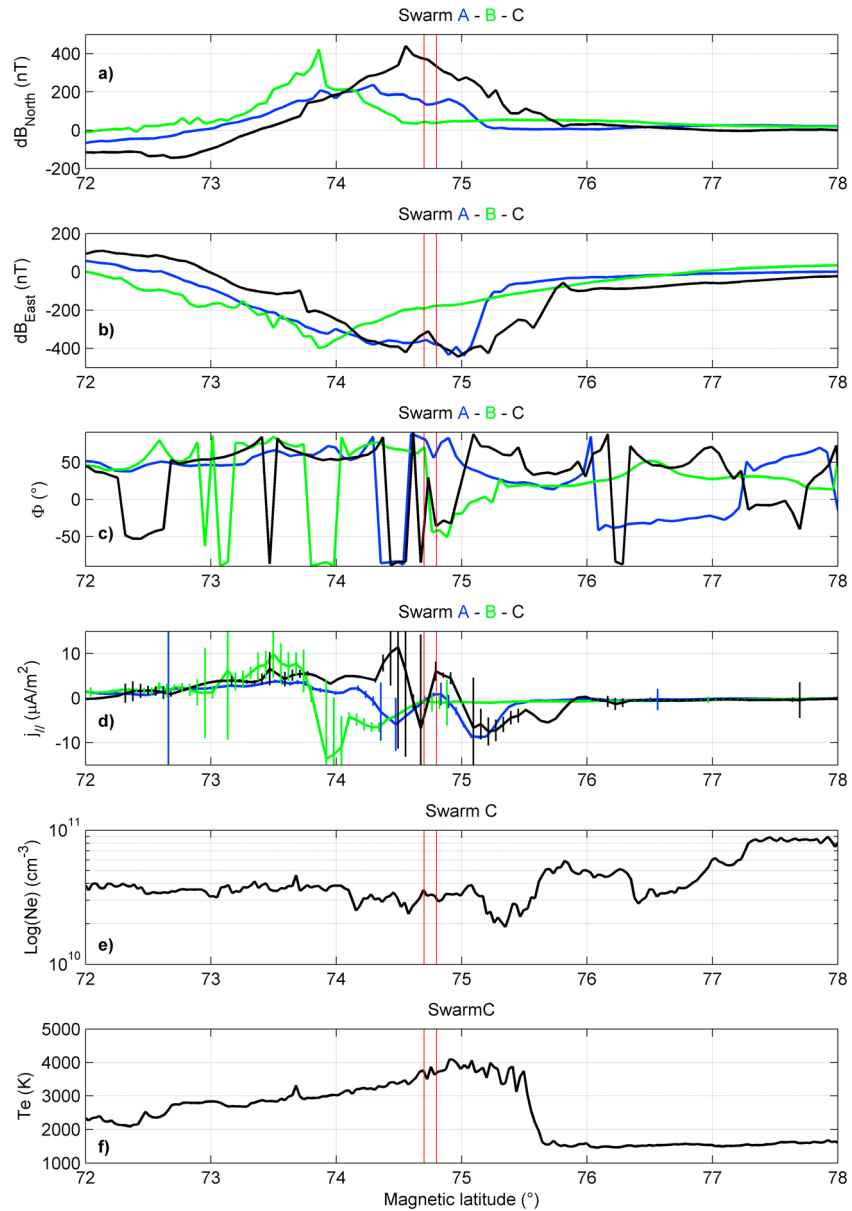
Figure 2. Swarms A (blue), B (green), and C (black) data with (a) the variation of the north and (b) east components of the magnetic field, (c) the angle Φ between the magnetic east and the current sheet directions, (d) the field-aligned current density derived from the VFM data (positive values are upward currents), and (e) the electron number density and (f) temperature recorded by the Langmuir probe versus magnetic latitude. The vertical red lines mark the edges of the ESR beam at 500 km.

Figures 2e and 2f show the electron density and temperature measured by the Langmuir probe on board Swarm C (plasma data are unfortunately not available on the two other satellites). When Swarm C flies over the ESR, around 20:29 UT, electron densities of the order of 3×10^{10} part/m^{-3} are recorded, while the electron temperature jumps from about 1500 K north of the ESR up to 4000 K near the radar. This latter transition is quite sharp and corresponds, in time, to the intensification of the aurora (Figure 1d).

Within the FAC structure crossed by Swarm C, the spacecraft flies between 75.5° and 75° latitude through a region of globally downward FAC with the electron temperature varying around 3500 K, which is surprisingly high. Then, between ~75.7° and 75.5° is a crossed region of clear upward FAC where T_e exceeds 4000 K when the FAC density is the highest, as expected. Then at slightly lower latitudes, either the FAC is estimated with such an error that it is impossible to affirm its direction or it is slightly upward,

hence the smaller T_e. The global trend (high T_e for upward FAC and lower T_e for downward FAC) is observed but likely due to the error made on the FAC density, the one-to-one correspondence between the FAC direction and the measured electron temperature is not always straightforward.

2.4. ESR Data Analysis

On 9 January 2014, the ESR was operated as a common program and we use in this study the data from the 42 m dish, the one constantly pointing along the local magnetic field line (azimuth 184.5°, elevation 81.6°). The data were analyzed with the GUISDAP software [*Lehtinen and Huuskonen*, 1996] with an integration time of 1 min and an altitude domain between 80 and 465 km, divided in 32 range gates.

Figures 1e–1h show the electron number density, the electron temperature, the ion temperature, and the field-aligned ion velocity, as functions of altitude and universal time. Before 20:20 UT, the radar observes a relatively quiet and cold ionosphere with an F region peaking at about 2×10^{11} part/m^3 at 260 km altitude and with an electron temperature remaining around 1000 K. Then, at 20:20 UT, the electron temperature starts to increase, while the E region becomes denser; this indicates that precipitation of energetic (typically keV) particles occurs. This coincides with the start of the auroral intensification seen in MSP data (Figure 1d). Then, between 20:22 and 20:27 UT, a more tenuous ($N_e \sim 10^{11}$ part/m^3) and cold ($T_e \sim 1500$ K in the F region) ionosphere is observed. From 20:28 UT, the ionosphere becomes hotter and denser, with N_e peaking at 9×10^{11} part/m^3 at 105 km and reaching 5×10^{11} part/m^3 at 250 km, and the electron temperature reaching 2500 K at 250 km and 3500 K at 450 km. These two regions could correspond to the downward and upward FAC region crossed by Swarm at 500 km. At ~ 20:26 UT, Swarm B crossed the downward FAC close to the ESR beam; then, as the current system moved to higher latitude, the ESR found itself in the region of upward FAC. In this latter region, the electron heat flux is directed toward the Earth and is very effective in heating the ionospheric electrons [*Banks et al.*, 1976; *Blelly and Alcaydé*, 1994; *Blelly et al.*, 1996], as measured by the ESR. (The reader should note that tenuous and cold ionosphere observed at 20:30 UT is an artifact due an error in the analysis.)

2.5. ESR Data Postanalysis

The determination of thermospheric parameters from incoherent scatter data is made possible via the postanalysis method described by *Blelly et al*. [2010]. In our case, it is valuable because we have used some of the outputs of this procedure for our simulation (next section). In fact, in addition to thermospheric parameters such as the neutral temperature and the transition region between molecular and atomic ions, this method also gives us the effective electric field responsible for the ion heating through frictional heating and the electron heat flux that applies on the last range gate (here corresponding to 465 km altitude).

For instance, around 20:29 UT, the downward electron heat flux reaches a maximum of the order of 40 μW/m^2, while the effective electric field reaches a maximum of 27 mV/m, in good agreement with the convection speed of about 500 m/s measured by the SuperDARN radars in the same area.

3. Ionospheric Modeling

3.1. TRANSCAR Model

TRANSCAR is an ionospheric model that consists, in the version used in this work, of a 13-moment fluid code coupled to a kinetic code. It is able to model the ionosphere between 90 and 3000 km altitude; its outputs include the plasma parameters measured by incoherent scatter radars: electron density and temperature as well as ion densities, temperatures, and velocities for the six ion species treated: H^+, O^+, N^+, O_2^+, N_2^+, and NO^+. For a complete description of the code, one can refer to *Diloy et al*. [1996], *Blelly et al*. [2005], and references therein.

Among the necessary inputs to the model, some may be supplied by measurements. The $F_{10.7}$ index is a proxy for the solar insolation and the corresponding ionization, the convection velocity is given by the SuperDARN radars. Regarding particle precipitation, when no satellite measured it in the vicinity, we need to adjust the typical energy and energy flux of the precipitating electrons (assuming a Maxwellian energy spectrum) to match as much as possible the observed profiles. In our case, the energy and energy flux were set to 3 keV and 10^8 keV/cm^2/s/sr to model the ionosphere around 20:26 UT when the downward FAC is supposed to stand above the radar, and to 1 keV and 10^9 keV/cm^2/s/sr around
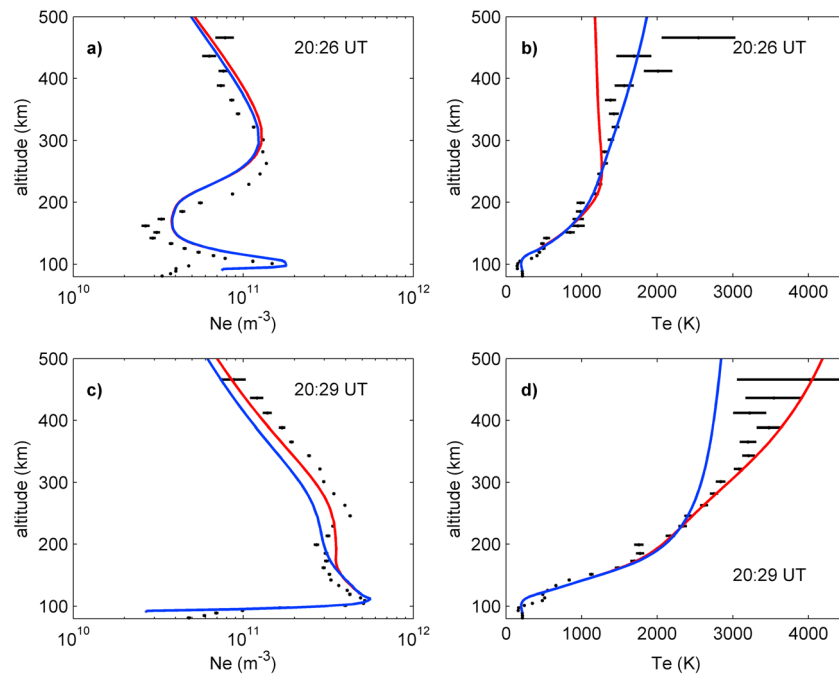
Figure 3. Measured (black bars) and modeled with (red lines) or without FAC (blue lines) altitude profiles of the (a, c) electron number density and (b, d) temperature at 20:26 UT (Figures 3a and 3b) and 20:29 UT (Figures 3c and 3d).

20:29 UT when the upward FAC is observed above the ESR. The electron heat flux applied at the top of our simulation domain (3000 km) is set to $-0.45\,\mu W/m^2$. At last, we have used an averaged FAC density and direction determined from Swarm (see previous section) as an input: we apply alternatively a $5\,\mu A/m^2$ downward current and $5\,\mu A/m^2$ upward currents. (More details on how we set up the input parameters may be found in *Pitout et al.* [2013]). For comparison purposes, we also run the model with no FAC in both cases.

3.2. Simulation Results

The results of our simulations are shown in Figure 3. Each of the four panels shows the density or temperature profiles observed by the ESR (black bars showing the error on the measurements) and two modeled profiles: one with a $\pm 5\,\mu A/m^2$ FAC (red), the other with no FAC (blue).

At 20:26 UT (Figures 3a and 3b), although Swarm A flies through a downward FAC very close to the ESR beam, we manage to reproduce the observed profiles without FAC (blue curve). This suggests that the downward FAC did not stand in the ESR beam long enough to affect the observed ionosphere. On the other hand, an upward FAC of $5\,\mu A/m^2$ is necessary to model the profiles at 20:29 UT (Figures 3c and 3d). While the overall shapes of the profiles are reproduced, we have differences in the electron density: we are 8% off in the E region, 25% off at most in the F region, and 3% off at the top altitude. The electron temperature is much better modeled with typical deviation below 5%, except for a few outliers around 400 km altitude. These errors allow us to quantitatively compare our modeling to the measurements within a margin of 25% at worst in the F region, below 10% everywhere else.

Along the field lines, the resulting heat flux that undergoes the ionosphere is the sum of the applied heat flux at the topside ionosphere and the contribution of the FAC (equation 5.56 in *Schunk* [1975]). We can compare quantitatively our modeling and the measurements by the ESR at 465 km, the highest altitude reached by the radar beam at which our postintegration method determines the heat flux. At this altitude, the simulation gives a value of $-25\,\mu W/m^2$ while the postanalysis of radar data (see section 2.5) gives $-40\,\mu W/m^2$ with an error of the order of $\pm 15\,\mu W/m^2$.

Regarding the charge carriers of the FAC, a $5\,\mu A/m^2$ current density requires a net particle flux of 3.1×10^{13} $q/m^2/s$. In the downward FAC, our modeling gives this latter value for the upward ionospheric electron

flux confirming that the downward current is entirely carried by up going ionospheric thermal electrons [*Hoffman et al.*, 1985]. In the upward FAC however, the downward thermal electron flux given by the model is ~1–2 × 10^{13} el/m^2/s, thus too small to account for the FAC density. Although both the ESR (Figures 1f and 1h) and the Electric Field Instrument on board Swarm C record upwelling ions (not shown), the upward ion flux given by our simulation is negligible and barely contribute to the overall current density. This indicated that precipitating electrons contribute significantly to the total current density as suggested by *Abe et al.* [1991].

4. Discussion

We would like to address two points in this section: the cause of the event we have observed and the quantitative comparison of the measurements made by Swarm and the ESR.

4.1. Pressure Pulse or/and Substorm Onset?

This event is undoubtedly closely related to the solar wind pressure pulse that hit the magnetosphere at 20:11:30 UT. Therefore, the observed features are either the direct consequences of the solar wind pressure pulse or due to a substorm triggered by the pressure pulse. Offhand, the fact that our observations are made at high latitude pleads for a pressure pulse effect but very high latitude substorms may occur [*Singh et al.*, 2012]. In favor of the substorm onset, we observe a sudden and intense brightening of the auroral display, followed by an apparent poleward expansion of the magnetic signature and of the auroral display [*Akasofu*, 1964; *Fujii et al.*, 1994] as recorded by the IMAGE ground magnetometers and the MSP. Yet, the elapsed time between the pressure pulse and the auroral brightening is very short, a few minutes, which is typical for a direct response of the coupled magnetosphere-ionosphere system to the pressure pulse [*Chua et al.*, 2001]. On the other hand, even if it takes more than 30 min to trigger a substorm by the classical loading/unloading of the magnetosphere [*Rostoker et al.*, 1987], the solar wind direct driving of a substorm can be much shorter: 10 min may suffice [*Zhou and Tsurutani*, 2001]. Even under IMF conditions which are a priori not too favorable (IMF-$Bz > 0$), substorms can be triggered [*Liang et al.*, 2004]. We feel we cannot conclude firmly on that. However, a clue is that electrons with energies greater than 10 keV are expected during a substorm [*Chua et al.*, 2001]. We have no indication that precipitation of so high-energy electrons occur in our case (we have successfully modeled profiles with 3 keV electrons at most).

4.2. ESR and Swarm Plasma Data Comparison

Such a conjunction is incidentally an excellent way to cross-calibrate spaceborne instruments like the Langmuir probes on board Swarm and incoherent scatter radars. Strictly speaking, we cannot directly compare measurements by the ESR and Swarm C because the radar pulse code used on 9 January 2014 allows a sounding up to 465 km altitude only. However, given the very close altitude of the Swarm satellites, 500 km, we can extrapolate altitude profiles given by the radar. Another limitation comes from the radar data integration time necessary to obtain an acceptable signal-to-noise ratio: 1 min.

At the top altitude sounded by the ESR, the electron density measured at 20:29 UT is 9×10^{10} part/m$^3 \pm 1 \times 10^{10}$ part/cm^3. We linearly extrapolate the two last points of the profile recorded by the ESR to find that the number density should be around 2×10^{10} part/cm^3 at 500 km with an error of the order of $\pm 1 \times 10^{10}$ part/cm^3 (error on N_e at 465 km). The Langmuir probe on board Swarm C measures electron number densities of 3×10^{10} part/cm^{-3} at 20:29 UT.

As for the temperatures, the linear extrapolation of the temperature profile recorded by the ESR at 20:29 UT gives a temperature of 4200 K (±1000 K) at 500 km altitude. The Langmuir probe on board Swarm C measures electron temperatures around 3600–3800 K when flying through the radar beam.

Consequently, as far as the measured electron number density and temperature are concerned, and considering the errors made on the ESR measurements (the processing of ESR data integrates raw data over a large volume of several kilometers in size at high altitude), we can conclude that the results agree within the ESR measurement errors and this comparison gives a first idea of systematic errors in uncorrected (uncalibrated) Langmuir probe data. As for the Langmuir probe in situ measurements, the error is expected to be much lower, a few percent typically.

5. Summary

On 9 January 2014, a pressure pulse impinges the magnetosphere at 20:11:30 UT. An immediate response is observed at 20:12 UT in ground magnetometers, followed by a delayed response at high latitudes where a westward Hall current appears and propagates northward while the auroral activity intensifies.

We have observed the ionospheric signature of particle precipitation and field-aligned currents associated with the compression of the magnetosphere or with a high-latitude substorm triggered by the pressure pulse. The associated FAC system as revealed by Swarm consists of a structure which is ~3° wide in latitude. The poleward part of the structure is a downward FAC region, and an upward FAC is found at lower latitude. This structure was seen to make an incursion in the ESR field of view. As a consequence, radar observations clearly show that the overall effect is an electron heating, that is well reproduced by our simulations. Besides, having an independently measured value of the FAC intensity by Swarm allows us to better constrain the input parameters to our numerical code, and, in turn, our code validates the current densities determined from Swarm data.

At last but not least, one of our goals was to show how successful and fruitful the association of the Swarm satellites, the ESR (or any other incoherent scatter radar), and the TRANSCAR model can be in (i) observing the temporal evolution of a FAC system and (ii) studying the ionospheric thermodynamics and electrodynamics associated with this FAC system.

References

Abe, T., T. Okuzawa, K. Oyama, H. Fukunishi, and R. Fujii (1991), Variations of thermal electron energy distribution associated with field-aligned currents, *Geophys. Res. Lett.*, *18*, 348–352, doi:10.1029/91GL00033.

Akasofu, S. I. (1964), The development of the auroral substorm, *Planet. Space Sci.*, *12*, 273–282.

Anderson, B. J., H. Korth, C. L. Waters, D. L. Green, and P. Stauning (2008), Statistical Birkeland current distributions from magnetic field observations by the Iridium constellation, *Ann. Geophys.*, *26*, 671–687, doi:10.5194/angeo-26-671-2008.

Anderson, B. J., H. Korth, C. L. Waters, D. L. Green, V. G. Merkin, R. J. Barnes, and L. P. Dyrud (2014), Development of large-scale Birkeland currents determined from the Active Magnetosphere and Planetary Electrodynamics Response Experiment, *Geophys. Res. Lett.*, *41*, 3017–3025, doi:10.1002/2014GL059941.

Angelopoulos, V. (2008), The THEMIS mission, *Space Sci. Rev.*, *141*, 5–34, doi:10.1007/s11214-008-9336-1.

Angelopoulos, V. (2011), The ARTEMIS mission, *Space Sci. Rev.*, *165*, 3–25, doi:10.1007/s11214-010-9687-2.

Banks, P. M., R. W. Shunck, and W. J. Raitt (1976), The topside ionosphere: A region of dynamic transition, *Annu. Rev. Earth Planet. Sci.*, *4*, 381–440.

Blelly, P.-L., and D. Alcaydé (1994), Electron heat flow in the auroral ionosphere inferred from EISCAT-VHF observations, *J. Geophys. Res.*, *99*, 13,181–13,188, doi:10.1029/93JA03493.

Blelly, P.-L., A. Robineau, J. Lilensten, and D. Lummerzheim (1996), 8-moment fluid models of the terrestrial high-latitude ionosphere between 100 and 3000 km, in *Solar Terrestrial Energy Program (STEP): Handbook of Ionospheric Models*, edited by R. W. Schunk, pp. 53–72, Scientific Committee on Solar-Terrestrial Physics (SCOSTEP), Boulder, Colo.

Blelly, P.-L., C. Lathuillère, B. Emery, J. Lilensten, J. Fontanari, and D. Alcaydé (2005), An extended TRANSCAR model including ionospheric convection: Simulation of EISCAT observations using inputs from AMIE, *Ann. Geophys.*, *23*, 419–431.

Blelly, P.-L., D. Alcaydé, and A. P. van Eyken (2010), A new analysis method for determining polar ionosphere and upper atmosphere characteristics from ESR data: Illustration with IPY period, *J. Geophys. Res.*, *115*, A09322, doi:10.1029/2009JA014876.

Chua, D., G. Parks, M. Brittnacher, W. Peria, G. Germany, J. Spann, and C. Carlson (2001), Energy characteristics of auroral electron precipitation: A comparison of substorms and pressure pulse related auroral activity, *J. Geophys. Res.*, *106*(A4), 5945–5956, doi:10.1029/2000JA003027.

Diloy, P.-Y., A. Robineau, J. Lilensten, P.-L. Blelly, and J. Fontanari (1996), A numerical model of the ionosphere, including the E-region above EISCAT, *Ann. Geophys.*, *14*, 191.

Dunlop, M. W., and A. Balogh (1993), On the analysis and interpretation of four spacecraft magnetic field measurements in terms of small scale plasma processes, in *Spatio-Temporal Analysis for Resolving Plasma Turbulence (START)*, pp. 223–231, Eur. Space Agency WPP, ESA WPP-047, Paris.

Friis-Christensen, E., H. Lühr, D. Knudsen, and R. Haagmans (2008), Swarm—An Earth Observation Mission investigating Geospace, *Adv. Space Res.*, *41*, 210–216.

Fujii, R., R. A. Hoffman, P. C. Anderson, J. D. Craven, M. Sugiura, L. A. Frank, and N. C. Maynard (1994), Electrodynamic parameters in the nighttime sector during auroral substorms, *J. Geophys. Res.*, *99*, 6093–6112, doi:10.1029/93JA02210.

Greenwald, R. A., et al. (1995), DARN/SuperDARN: A global view of the dynamics of high-latitude convection, *Space Sci. Rev.*, *71*, 761–796.

Hoffman, R. A., M. Suguira, and N. C. Maynard (1985), Current carriers for the field-aligned current system, *Adv. Space Res.*, *5*, 109–126.

Iijima, T., and T. A. Potemra (1976), The amplitude distribution of field-aligned currents at northern high latitudes observed by Triad, *J. Geophys. Res.*, *81*, 2165–2174, doi:10.1029/JA081i013p02165.

Iijima, T., and T. A. Potemra (1978), Large-scale characteristics of field-aligned currents associated with substorms, *J. Geophys. Res.*, *83*, 599–615, doi:10.1029/JA083iA02p00599.

Lehtinen, M. S., and A. Huuskonen (1996), General incoherent scatter analysis and GUISDAP, *J. Atmos. Sol. Terr. Phys.*, *58*, 435–452.

Liang, J., G. J. Sofko, E. F. Donovan, M. Watanabe, and R. A. Greenwald (2004), Convection dynamics and driving mechanism of a small substorm during dominantly IMF By+, Bz + conditions, *Geophys. Res. Lett.*, *31*, L08803, doi:10.1029/2003GL018878.

Lühr, H. (1994), The IMAGE magnetometer network, *STEP International*, *4*, 4–6.

Marchaudon, A., J.-C. Cerisier, J.-M. Bosqued, C. J. Owen, A. N. Fazakerley, and A. D. Lahiff (2006), On the structure of field-aligned currents in the mid-altitude cusp, *Ann. Geophys.*, *24*, 3391–3401.

Marchaudon, A., J.-C. Cerisier, M. W. Dunlop, F. Pitout, J.-M. Bosqued, and A. N. Fazakerley (2009), Shape, size, velocity and field-aligned currents of dayside plasma injections: A multi-altitude study, *Ann. Geophys.*, *27*, 1251–1266.

Olsen, N., et al. (2013), The Swarm Satellite Constellation Application and Research Facility (SCARF) and swarm data products, *Earth Planets Space*, *65*, 1189–1200, doi:10.5047/eps.2013.07.001.

Pitout, F., P. Eglitis, and P.-L. Blelly (2003), High-latitude dayside ionosphere response to Pc5 field line resonance, *Ann. Geophys.*, *21*, 1509–1520.

Pitout, F., P.-L. Blelly, and D. Alcaydé (2013), EISCAT observations and TRANSCAR simulation of the solar eclipse of 1 August 2008, *JASTP*, *105–106*, 336–349, doi:10.1016/j.jastp.2013.02.004.

Ritter, P., H. Lühr, and J. Rauberg (2013), Determining field-aligned currents with the Swarm constellation mission, *Earth Planets Space*, *65*, 1285–1294.

Robert, P., and A. Roux (1993), Dependence of the shape of the tetrahedron on the accuracy of the estimate of the current density, in *Spatio-Temporal Analysis for Resolving Plasma Turbulence (START)*, pp. 289, Eur. Space Agency WPP, ESA WPP-047, Paris.

Rostoker, G., S.-I. Akasofu, W. Baumjohann, Y. Kamide, and R. L. McPherron (1987), The roles of direct input of energy from the solar wind and unloading of stored magnetotail energy in driving magnetospheric substorms, *Space Sci. Rev.*, *46*, 93–111.

Röttger, J., U. G. Wannberg, and A. P. van Eyken (1995), The EISCAT scientific association and the EISCAT Svalbard radar project, *J. Geomagn. Geoelectr.*, *47*, 669–679.

Schunk, R. W. (1975), Transport equations for aeronomy, *Planet. Space Sci.*, *23*, 437–485.

Singh, A. K., A. K. Sinah, R. Rawat, B. Jayashree, B. M. Pathan, and A. Dhar (2012), A broad climatology of very high latitude substorms, *Adv. Space Res.*, *50*(11), 1512–1523.

Trattner, K. J., S. M. Petrinec, S. A. Fuselier, and T. D. Phan (2012), The location of reconnection at the magnetopause: Testing the maximum magnetic shear model with THEMIS observations, *J. Geophys. Res.*, *117*, A01201, doi:10.1029/2011JA016959.

Winglee, R. M., and J. D. Menietti (1998), Auroral activity associated with pressure pulses and substorms: A comparison between global fluid modeling and Viking UV imaging, *J. Geophys. Res.*, *103*, 9189–9205, doi:10.1029/97JA03732.

Zhou, X., and B. T. Tsurutani (2001), Interplanetary shock triggering of nightside geomagnetic activity: Substorms, pseudobreakups, and quiescent events, *J. Geophys. Res.*, *106*, 18,957–18,967, doi:10.1029/2000JA003028.